calcite crystals. Although Fuchigami and Sasaki (2005) expressed M + 3 layer as "irregular spherulitic prismatic structure," there are few characteristics on the cross-sectional surfaces (Figure 2–21C), as reported by Suzuki et al. (2010). Figure 2–21D shows the cross sections etched by 0.5 M EDTA, and insoluble membranous/fibrous OMs were also observed inside the crystals. But the amount of OMs is quite smaller in *Collisella* than any other shells in this study, which is comparable with fewer Fresnel contrasts in under-focused TEM images of *Collisella* than other shells (Figure 2–14B).

The prismatic structure of *Atrina* has a structure similar to that of *Pinctada* and *Pteria*, in which columnar calcite crystals are surrounded by thick organic walls and grow in the direction perpendicular to the shell surfaces (Figure 2–22A and 2–22C). The distinctive feature of *Atrina* is that each prism is composed of a single crystal though it also has as large amount of OMs as *Pinctada* inside the crystals. No insoluble OMs were observed in both the inner surfaces and cross sections etched by 0.5 M EDTA for 30 minutes. Instead, a lot of minute facets of calcite {104} planes appeared (Figure 2–22B and 2–22D). The etched fracture surfaces of Iceland spar showed similar facets to *Atrina* (Figure 2–22F and 2–22G), indicating that the prisms of *Atrina* are almost ideal single crystals. However, thin fibrous insoluble OMs were observed in the prisms etched by lower concentration (5 mM) of EDTA (Figure 2–22E). These thin fibrous OMs may correspond to the fibers that were reported by Nudelman et al. (2007) in a closely related shell, *Atrina rigida*. Considering these intracrystalline OMs are removed by the high concentration of EDTA, the mutual connection between them and/or the attachment to intercrystalline OMs are supposed to be weak in *Atrina* compared with other shells investigated.

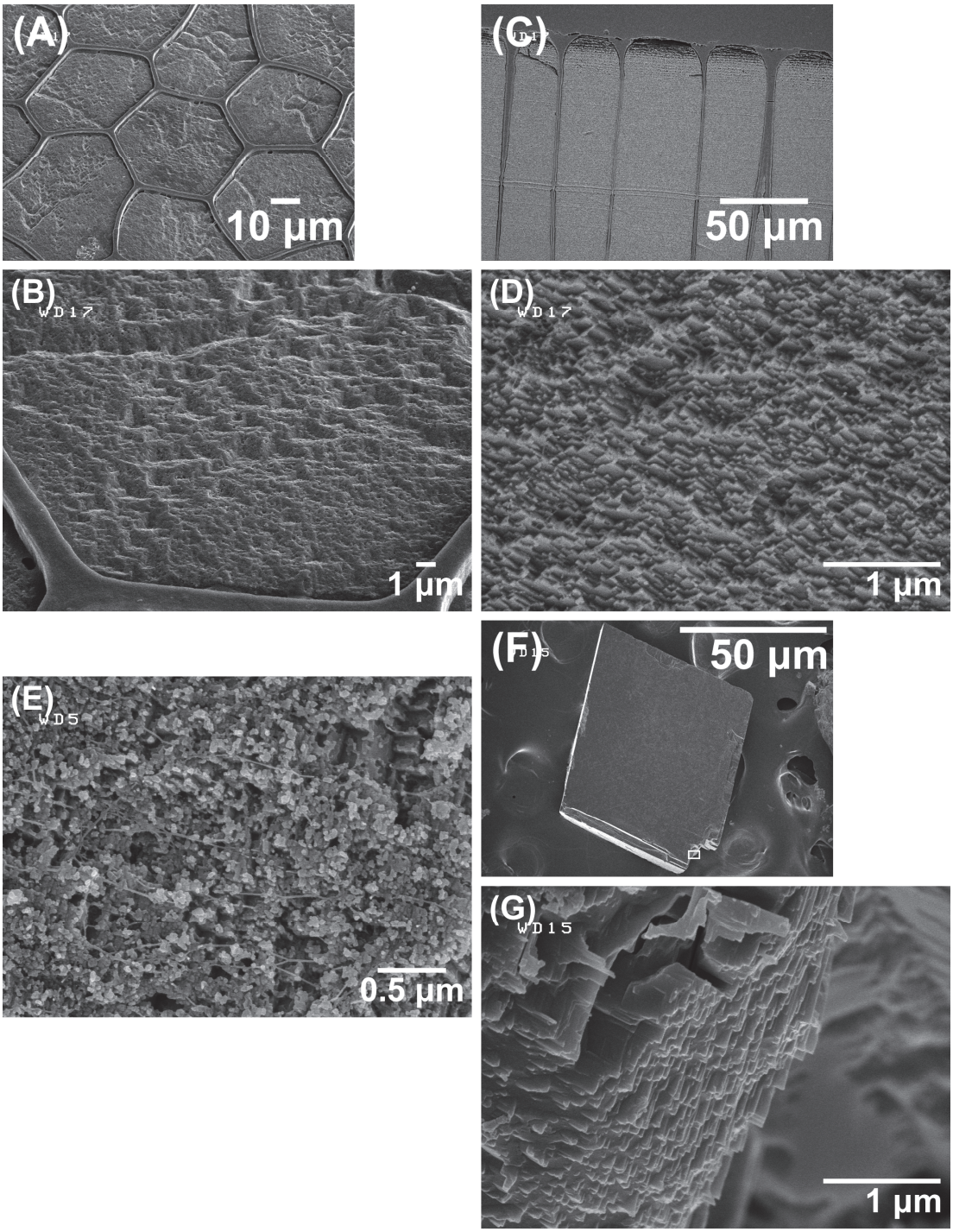

Figure 2–22. SEM images of *Atrina* and Iceland spar. Inner surfaces (A, B) and cross sections (C, D) of *Atrina* etched by 0.5 M EDTA for 30 minutes. (E) Inner surfaces of *Atrina* etched by 5 mM EDTA for 30 minutes. (F, G) Fractured Iceland spar etched by 0.5 M EDTA for 30 minutes. (G) is the enlarged view of the rectangle in (F).

2B.3.2 HAADF–STEM tomography

HAADF–STEM tomography was performed in order to verify whether membranous/fibrous insoluble OMs in SEM images are the same as intracrystalline OMs observed in TEM images or not. Since TEM images are just projections along an incident electron beam, HAADF–STEM tomography is beneficial to obtain 3D information. Although the contrast of HAADF–STEM images corresponds to atomic numbers, intracrystalline OMs are brighter in Figures 2–23 and 2–25 because the contrast was reversed for tomographic procedures. In the HAADF–STEM image of the prisms in *Pinctada*, aligned OMs divide crystals into sub-grains, as observed in TEM images (Figure 2–23e). When I tilted the specimen, fibrous organic networks like insoluble OMs in SEM images appeared (Figure 2–23a–d and 2–23f–i; supporting information (SI) Movie 1). Furthermore each sub-grain occasionally has different contrast intensity in SI Movie 1, which occurs because the crystal orientations of individual sub-grains are slightly different, and HAADF imaging cannot altogether avoid detecting coherently diffracted electrons. This phenomenon also proves that intracrystalline OMs induce small-angle misorientation in the crystals. Figure 2–24 is the 3D reconstructions of intracrystalline OMs generated from the tilt series of HAADF–STEM images. The interfaces between OMs and crystals were made brighter by using a 3D Sobel filter which is installed in the imaging processing software. The Sobel filter takes the local gradient of images and removes slowly varying backgrounds. The resulting images show bright boundaries tracing the interfaces between high and low intensity objects. The 3D reconstructions show the networks, and partly membranes, of OMs, though tiny OMs disappeared owing to the threshold condition (see also SI

Movie 2).

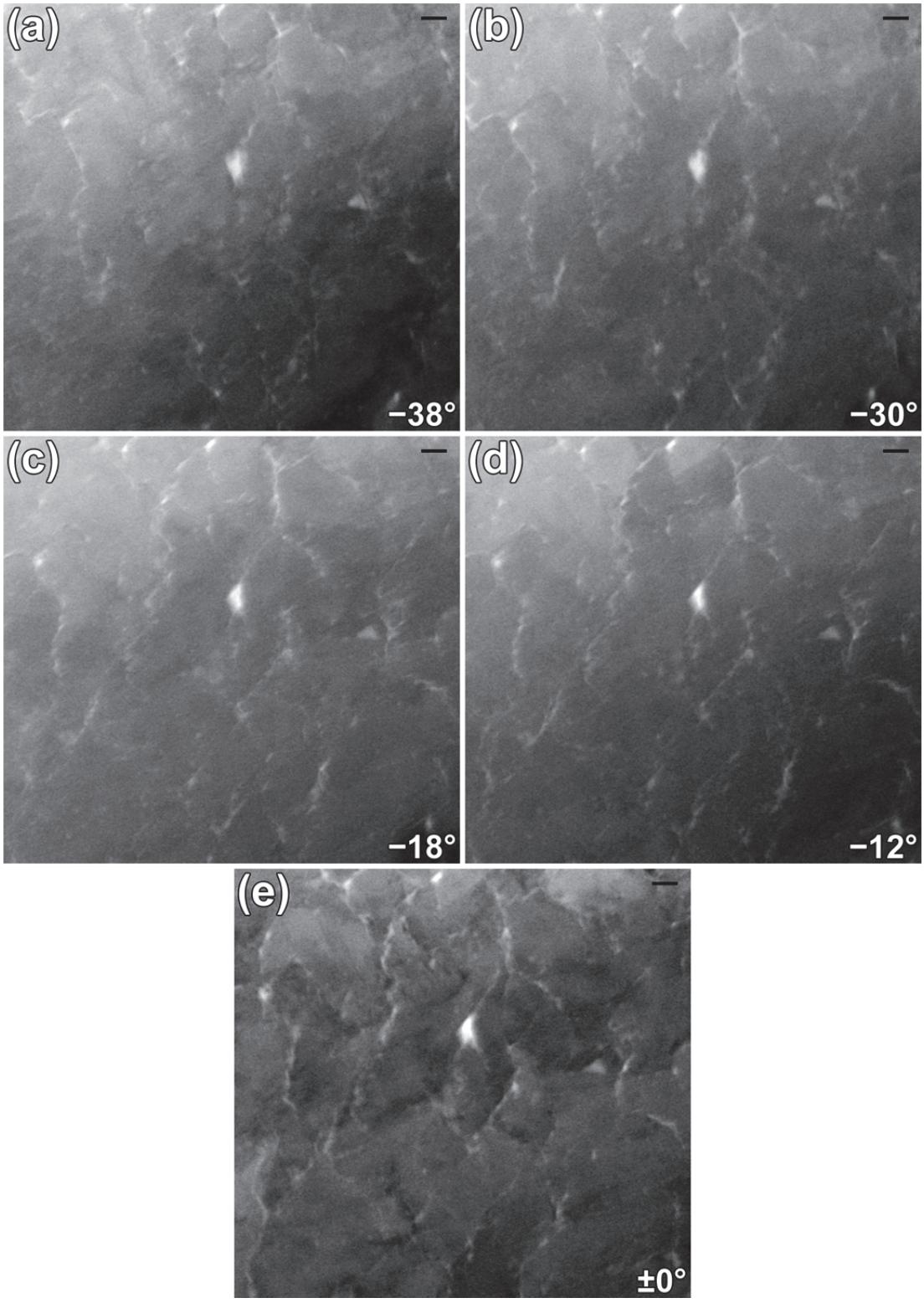

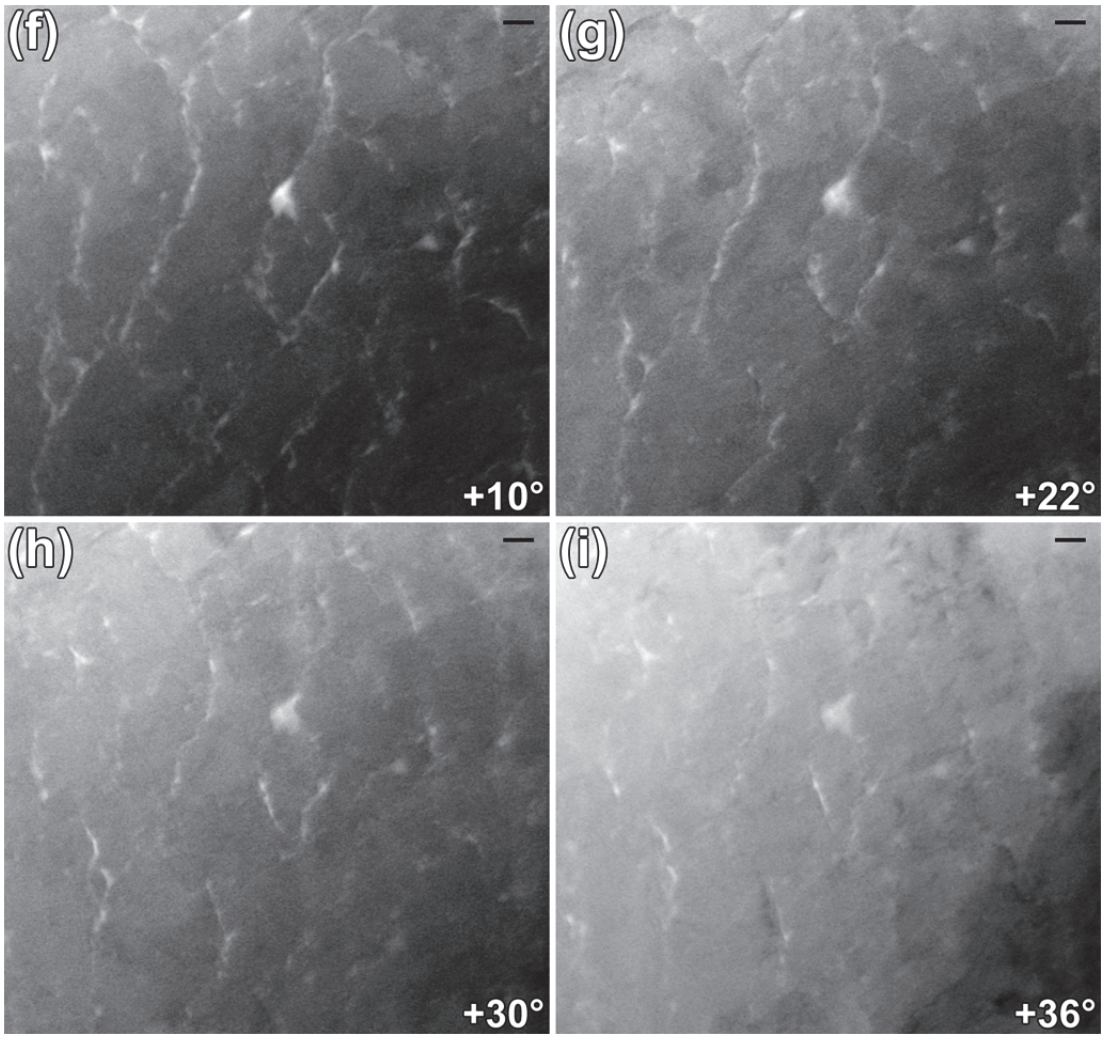

Figure 2–23. HAADF–STEM images of the prisms in *Pinctada*. Intracrystalline OMs show brighter contrast here because the contrast was reversed for tomographic procedures. The specimen of the images was tilted by −38° (a), −30° (b), −18° (c), −12° (d), ±0° (e), +10° (f), +22° (f), +30° (g), and +36° (h). Scale bar: 100 nm.

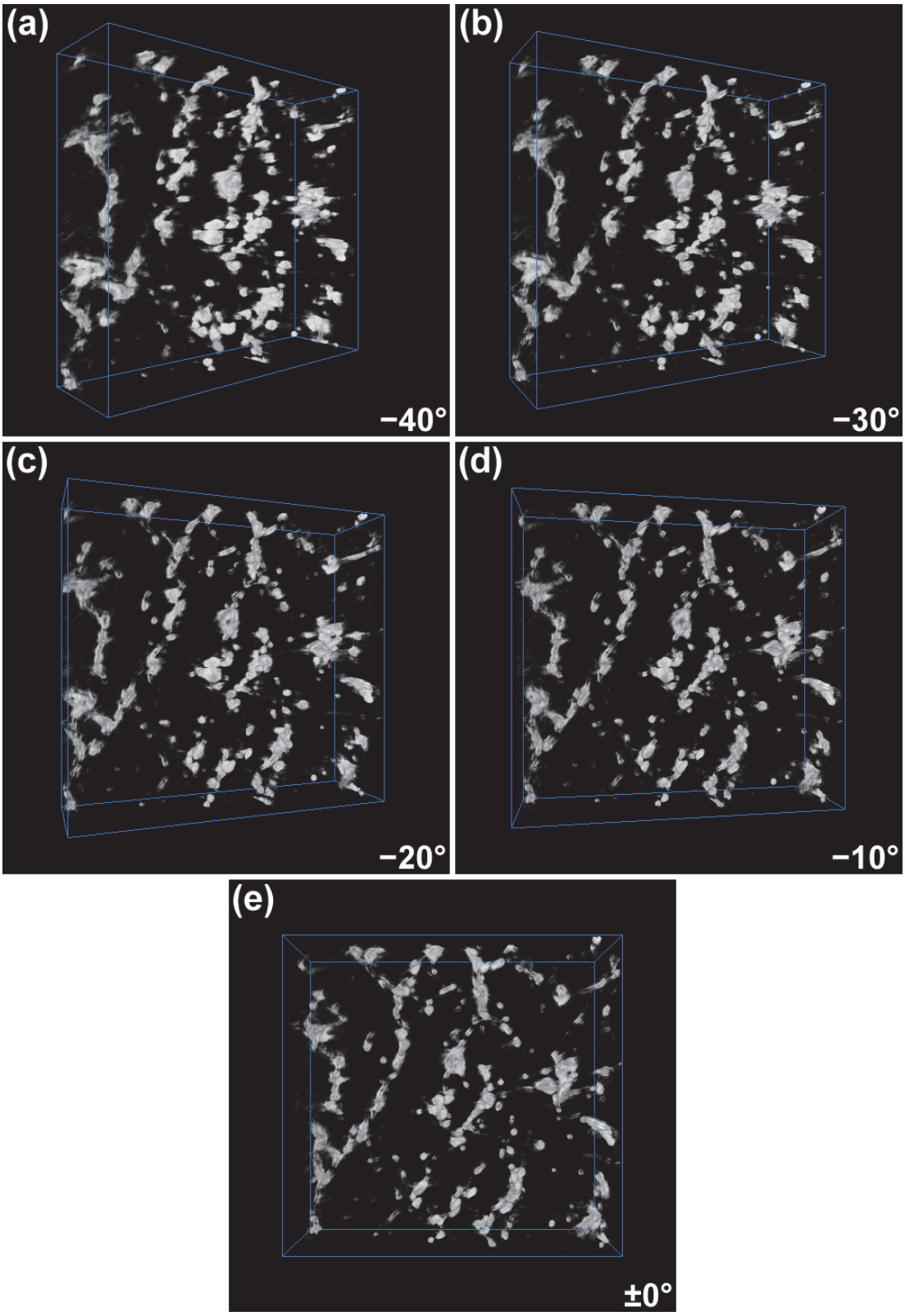
(a)
−40°
(b)
−30°
(c)
−20°
(d)
−10°
(e)
±0°

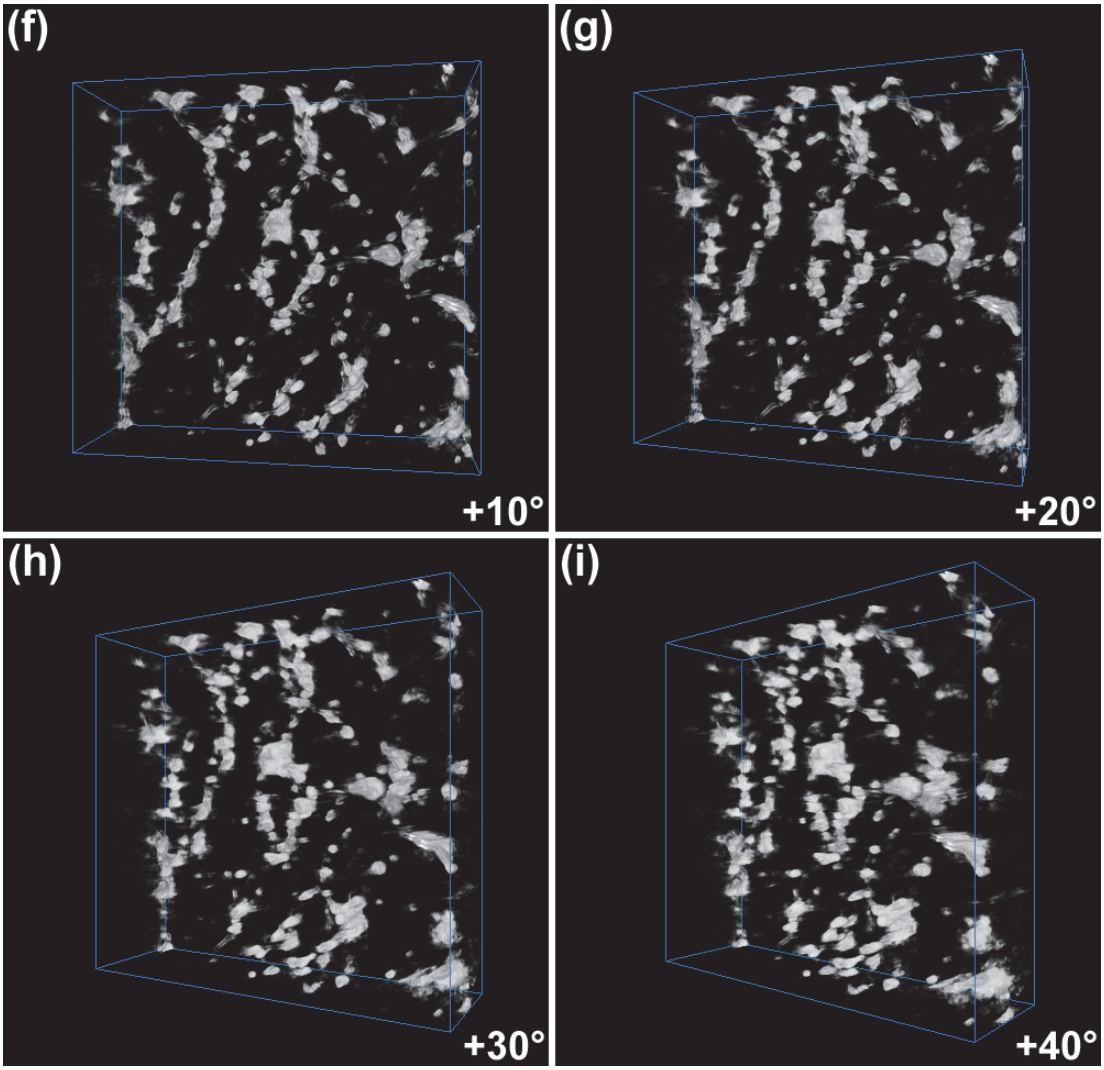

Figure 2–24. Three-dimensional reconstructions of intracrystalline OMs in the prisms of *Pinctada*., tilted by −40° (a), −30° (b), −20° (c), −10° (d), ±0° (e), +10° (f), +20° (g), +30° (h), and +40° (i).

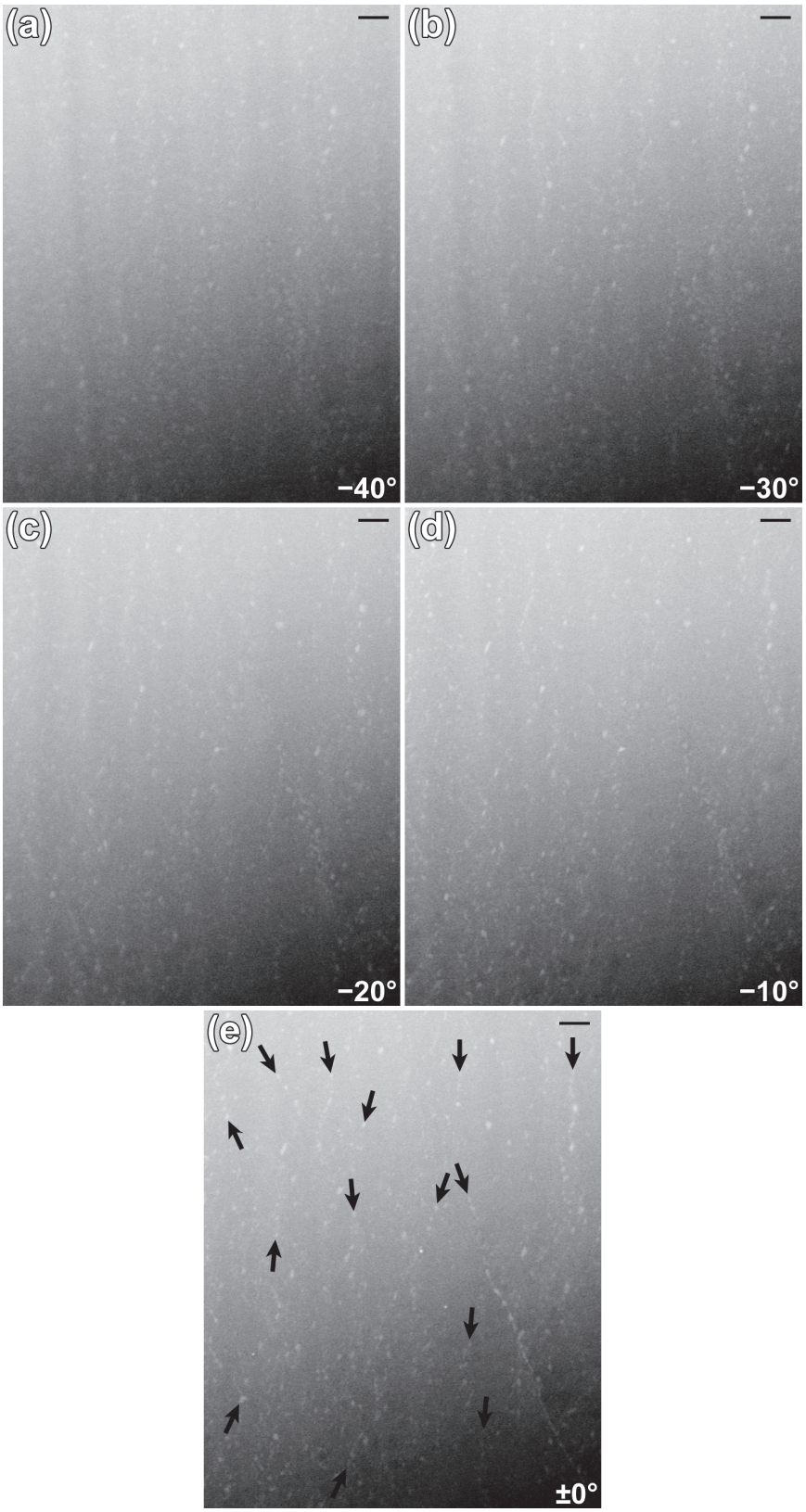
(a)
−40°
(b)
−30°
(c)
−20°
(d)
−10°
(e)
±0°

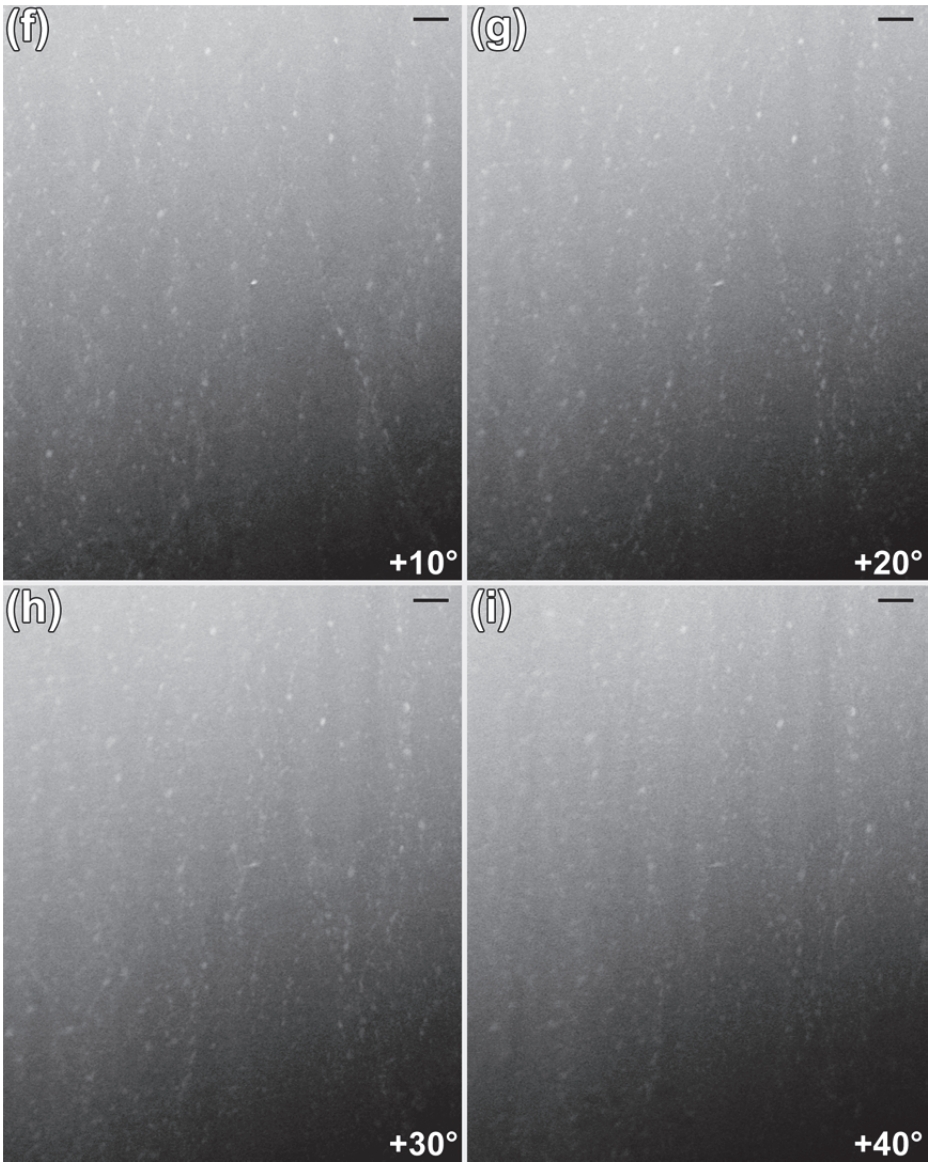

Figure 2–25. HAADF–STEM images of the prisms in *Atrina*. Intracrystalline OMs show brighter contrast here because the contrast was reversed for tomographic procedures. The specimen of the images was tilted by −40° (a), −30° (b), −20° (c), −10° (d), ±0° (e), +10° (f), +20° (g), +30° (h), and +40° (i). Scale bar: 100 nm. Arrows in (e) indicate spherular OMs that are elongated and aligned discontinuously like dotted lines.

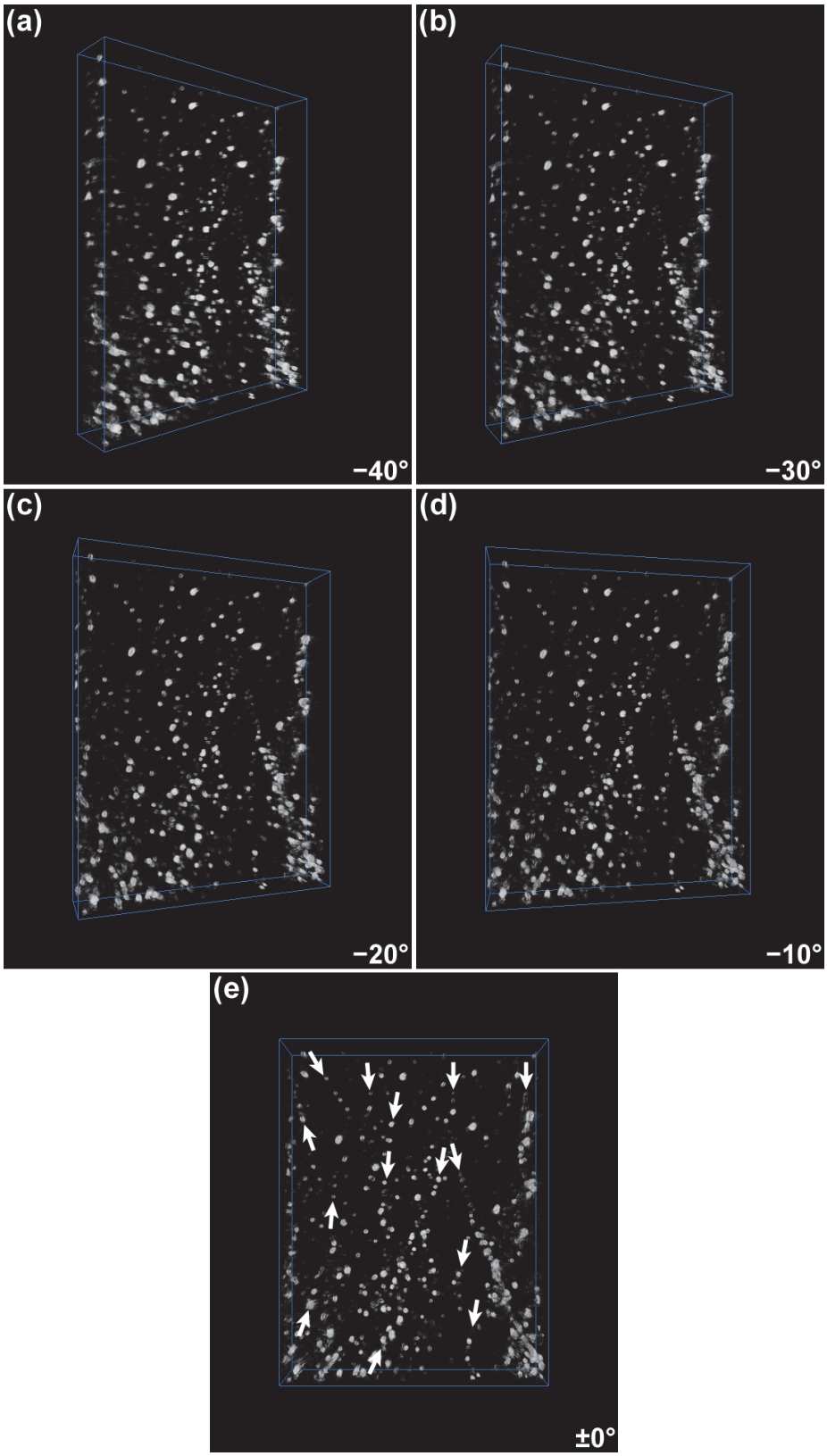
(a)
−40°
(b)
−30°
(c)
−20°
(d)
−10°
(e)
±0°

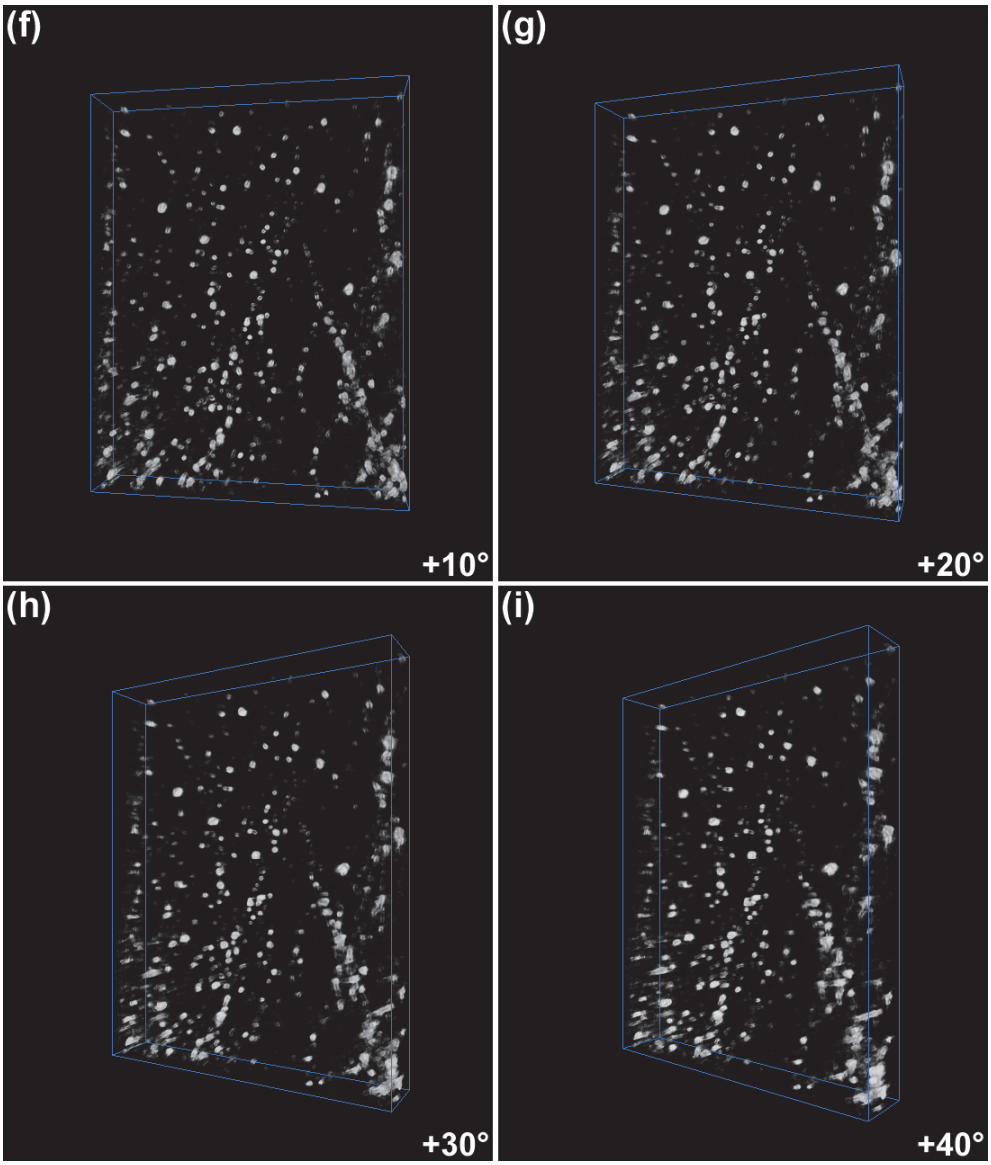

Figure 2–26. Three-dimensional reconstructions of intracrystalline OMs in the prisms of *Atrina*., tilted by −40° (a), −30° (b), −20° (c), −10° (d), ±0° (e), +10° (f), +20° (g), +30° (h), and +40° (i). Arrows in (e) indicate spherular OMs that are elongated and aligned discontinuously like dotted lines.

On the other hand, spherular OMs are homogeneously distributed inside crystals in the HAADF–STEM images of the prisms in *Atrina*, which is consistent with the results of TEM observation (Figure 2–25; SI Movie 3). However, intracrystalline OMs partially exhibit long thin shapes, which probably correspond to organic fibers observed using SEM in the prisms of *Atrina* etched by lower concentration of EDTA (Figure 2–22E). Besides many spherule-shaped OMs are elongated and aligned discontinuously like dotted lines. Hence I conclude that intracrystalline OMs in *Atrina* are not spherules but fibers. The elongated-spherular shapes were created by being cut off when thin TEM specimens were prepared using FIB. The 3D reconstructions confirm many dotted lines of OMs (Figure 2–26; SI Movie 4). These results indicate that insoluble organic fibers in SEM images are equivalent to intracrystalline OMs in TEM ones.

2B.4 Discussion

The outer calcite layers of both bivalve and gastropod shells except *Atrina* have membranous and net-like insoluble OMs inside the crystals, which induce sub-grain boundaries. Although the prisms of *Atrina* also contain insoluble OMs, they are shaped like thin fibers and have little influence on the crystal structure. Li et al. (2011) implied that the membranous and net-like shapes of insoluble OMs are artifacts formed by acid etching procedures. Instead, they suggested that organic nanopatches in TEM/STEM images reflect the real state of occluded OMs. Similar OMs to the nanopatches in the prisms of *Atrina rigida* were also observed in this study as spherules in those of *Atrina pectinata*. However, I insist that the spherular shapes were originated from the FIB

procedures in which organic thin fibers were cut irregularly during preparation of TEM specimens. Furthermore there may be one more reason why Li et al. could not observe continuous OMs in their samples using TEM. They made TEM specimens using FIB from the calcite prisms individually separated by dissolving interprismatic organic walls with an NaClO solution. I complementarily prepared TEM specimens from the individually separated prisms of *Crassostrea* in the same manner, but intracrystalline OMs were shaped like larger-sized spheres (Figure 2–27). The outcomes are totally different from my TEM observation in which continuous OMs were distributed perpendicular to the *c*-axes (Figure 2–12B). Therefore the treatment with an NaClO solution probably affects and dissolves not only interprismatic organic walls but also OMs that exist near the external surfaces of the prisms. Hence the integration of SEM and TEM imaging certainly indicates the shapes and distribution of insoluble OMs inside crystals.

Like interlamellar OMs of nacreous structure, the insoluble OMs may form

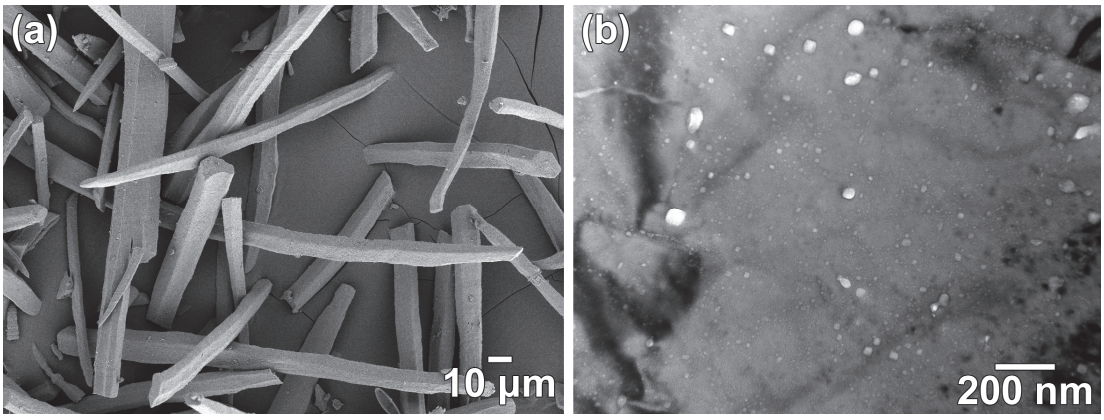

Figure 2–27. (a) SEM image of the prisms of *Crassostrea*, after the treatment of the prismatic layers with an NaClO solution. Interprismatic organic walls were completely dissolved and individual prisms separated. (b) Under-focused TEM image of the prisms in *Crassostrea*. The thin specimen for TEM were prepared from the separated prisms in (a) using FIB.

frameworks in which crystals grow because they are structurally preserved by themselves even though crystals dissolve and disappear owing to the decalcification treatment. Interprismatic organic walls are formed as frameworks before calcite deposition in the prismatic structure. The holey-membranous networks may also form frameworks inside the regions surrounded by the walls. Furthermore insoluble OMs generate sub-grain boundaries not only in bivalve but also in gastropod shells, implying such defective structure is a common feature of calcite crystals constituting outer layers of mollusk shells.

2.2 Chapter discussion

In this chapter, I focused on the calcite crystals that constitute the outer layers of mollusk shells, and their microstructures were investigated mainly using electron microscopy. The crystallographic characteristics of the calcite crystals were described in Chapter 2A, and the shapes and 3D distribution of intracrystalline OMs were revealed in Chapter 2B. The combined results indicated that all investigated shells except *Atrina* possess membranous and/or net-like insoluble OMs inside the crystals, which generate sub-grain boundaries and local lattice strain around them. The insoluble OMs may be pre-formed as a part of the framework structure in which crystals grow. Since the insoluble OMs exist before crystal deposition, they may interrupt crystal growth. The interruption is mainly due to physical blockage, not chemical inhibition, because insoluble OMs play a role of supplying environment of crystal formation rather than interacting with crystals as stated above. When the crystals further grow to incorporate the interruptive insoluble OMs, sub-grain boundaries are induced there. The defective structure due to the misorientation imposes lattice strain on the crystals, and furthermore, inhibits the propagation of the cleavages along calcite {104} planes. Considering that diverse mollusk shells develop such a structure–property relationship, the defective structure generated by small-angle misorientation may be a character acquired in the course of evolution for protecting their bodies.

On the other hand, though insoluble OMs exist also in the prisms of *Atrina*, they are thin fibrous shaped and easily removed by etching. Since such OMs cannot generate sub-grain boundaries like other shells, the prisms are monolithic single crystals. Therefore *Atrina* is inferior in mechanical properties to other shells. Instead, *Atrina*

shells grow very rapidly and reach to almost 20 cm in length within 2 years (Hendriks et al., 2012; Silina, 2012). *Atrina* shells may develop a strategy in which they enlarge and thicken their shells by increasing the crystal growth rate rather than designing the microstructure for improving their mechanical properties. In addition, even though the insoluble OMs in *Atrina* are not interconnected and easily disrupted, the crystals definitely contain OMs inside, which may result in a higher hardness value than geological calcite crystals, Iceland spar (Kunitake et al., 2013).

I revealed that insoluble OMs generate sub-grain boundaries in the shells investigated except *Atrina*. Now what is the difference between OMs in *Atrina* and other shells? Although the insoluble OMs in *Atrina* are shaped like thinner fibers, it is not clear whether the shapes are related to the disappearance of the sub-grain structure or not. This chapter described that insoluble OMs definitely have influence on crystal structure, but what roles do soluble OMs have? In Chapter 3, the influence of soluble OMs on crystal structure is examined through *in vitro* experiments.

2.3 Conclusions

The calcite crystals constituting the outer layers of diverse mollusk shells have membranous and net-like intracrystalline OMs, which are a part of organic frameworks formed before crystal precipitation. Such insoluble OMs induce sub-grain boundaries in the crystals, with gradual orientation change. Therefore I conclude that the intracrystalline OMs are elaborately incorporated into crystals and form intricate microstructures in biogenic calcite, which improve the mechanical properties of the crystals by inhibiting the propagation of cleavages along {104} planes. This mechanism for forming the microstructures elucidated in this study could lead to creating organic–inorganic composites with distinct structures and mechanical properties.

Chapter 3.

Effects of soluble organic molecules on microstructures in synthesized calcite crystals *in vitro*

3.1 Introduction

To investigate the interaction between crystals and OMs, *in vitro* syntheses of calcium carbonate crystals in the presence of various OMs have been conducted (Mann et al., 1990; Albeck et al., 1993, 1996a, 1996b; Didymus et al., 1993; DeOliveira and Laursen, 1997; Kim et al., 2011). Such *in vitro* experiments have been conducted with the OMs extracted by decalcification of calcium carbonate biominerals using acid or EDTA (acid/EDTA-soluble OMs). Syntheses of calcite crystals have been performed also in the presence of insoluble OMs. Although most of the insoluble OMs inside calcite crystals of mollusk shells are regarded as chitin, Li and his coworkers formed calcite crystals that contain agarose inside them instead of chitin (Li and Estroff, 2009; Li et al., 2009; Asenath-Smith et al., 2012). When a hot solution in which agarose is dissolved is cooled to ambient temperature, the solution turns into a gel. The agarose gel has net-like structure similar to insoluble OMs observed using SEM in Chapter 2B. The agarose gel

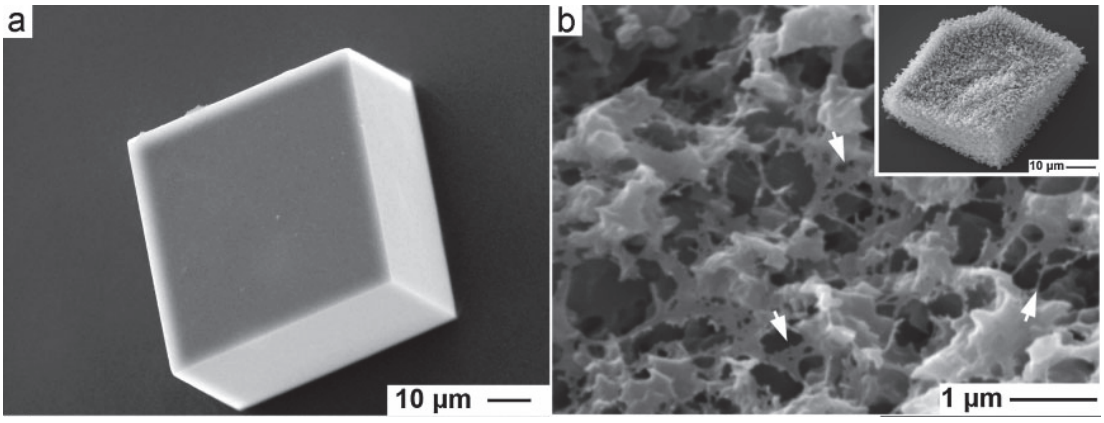

Figure 3–1. (a) SEM image of calcite crystals grown in an agarose gel. (b) SEM image of the etched surface of the crystal in (a) with deionized water for 4 days. White arrows highlight the incorporated gel fibers. (Li and Estroff, 2009).

is incorporated into the crystals that are synthesized inside the gel when the gel strength and the crystal growth rate is high (Figure 3–1; Li and Estroff, 2009). The composites of crystals and insoluble OMs have been produced to date with such a hydrogel. However, the calcite crystals formed with the agarose gel maintain a perfect single-crystalline character though large amount of agarose is incorporated into the crystals (Figure 3–2; Li et al., 2009). The interfaces between the agarose fibers and the calcite crystals showed not only {104} planes as low-energy facets but also high-energy facets such as {012} planes. They formed concave growth fronts at the internal surfaces, probably because the crystals grow around the fibers to incorporate them. Therefore insoluble OMs interrupt crystal growth as physical blockage, which is still unable to induce crystal defects such as sub-grain boundaries and dislocation. I complementarily synthesized calcite crystals with an agarose gel in the same manner as Li and Estroff (2009). The under-focused TEM image of the synthesized crystals verified the existence of the agarose fibers inside the crystals, but smooth bend contours were also observed, indicating that the crystals are monolithic single crystals without any defective structures (Figure 3–3). Williamson–Hall plots obtained from XRD measurements also showed that the synthesized crystals possess no local lattice strain.

On the other hand, the calcite crystals that contain soluble OMs were also formed in many studies, and their structure has been examined. For instance, a protein, caspartin, which was identified from calcite prismatic layers in *Pinna nobilis*, is incorporated into calcite crystals, which consequently generates lattice distortion (Pokroy et al., 2006b). Furthermore Borukhin et al. (2012) showed that even a single amino acid can induce similar lattice distortion. Figure 3–4 indicates (104) calcite reflections in XRD profiles obtained from the crystals synthesized in the presence of

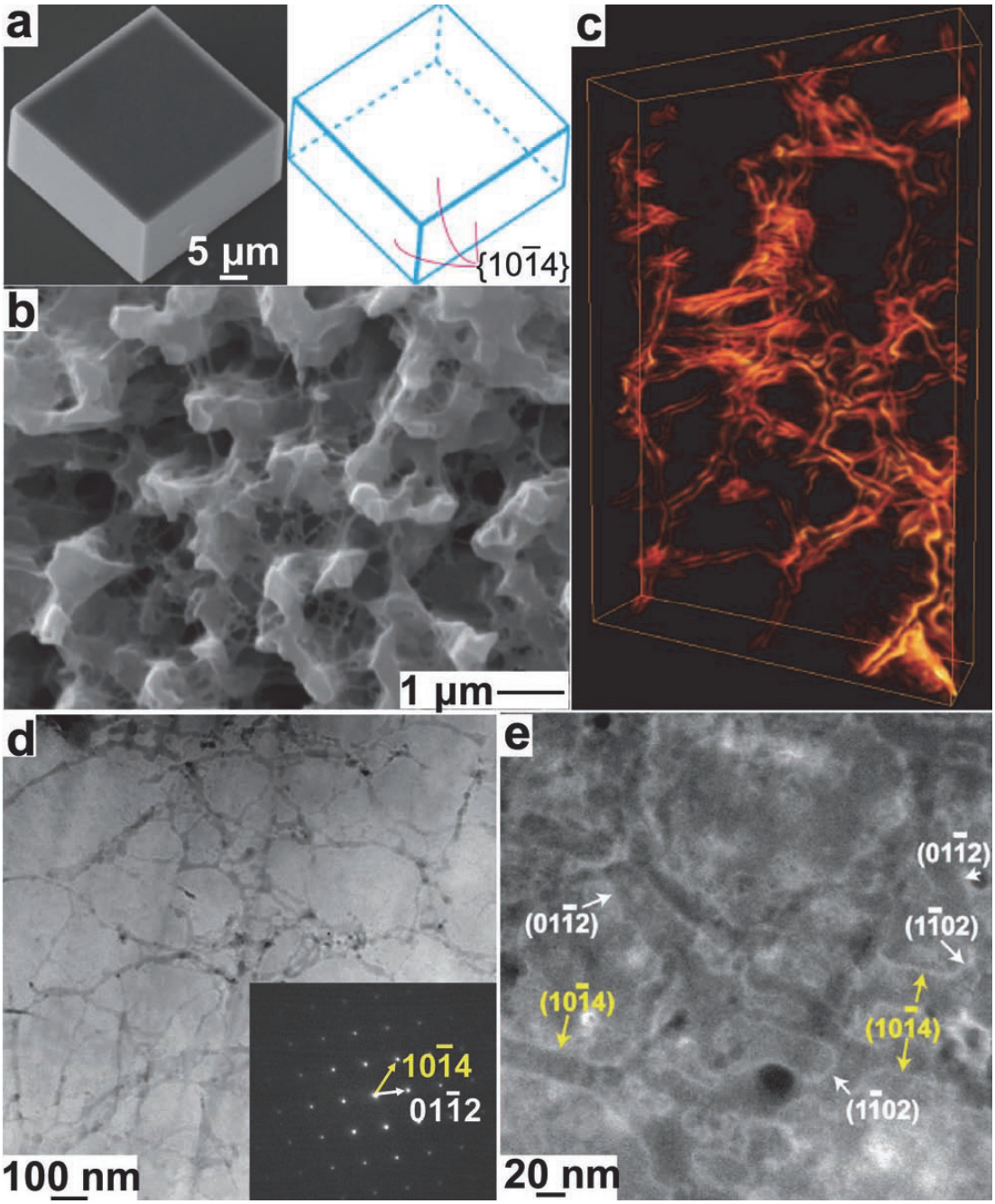

Figure 3–2. (a) SEM image of a calcite crystal grown in an agarose gel and a model of a calcite crystal expressed by six {104} faces. (b) SEM image of the calcite crystal in (a) after etching in deionized water for 4 days. (c) Electron tomography reconstruction of randomly distributed agarose networks inside the calcite crystal. (d) ADF–STEM image of a thin specimen prepared from the calcite crystal using FIB. Inset shows a SAD pattern. (e) Enlarged ADF–STEM image. The interfaces between the crystal and agaose fibers are partially indexed. (Asenath-Smith et al., 2012).

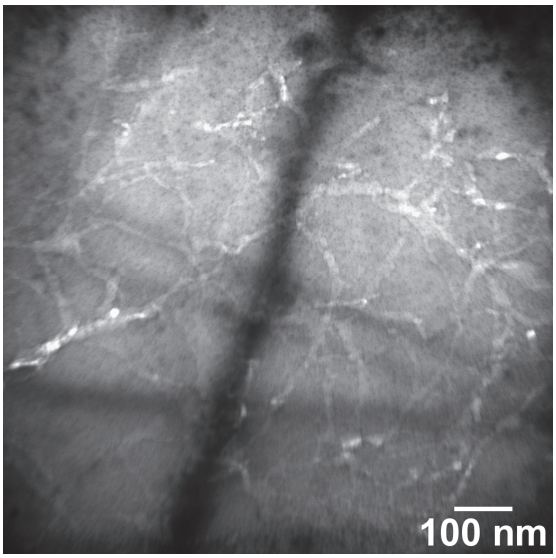

Figure 3–3. Under-focused TEM image of the synthesized calcite crystal with the agarose gel.

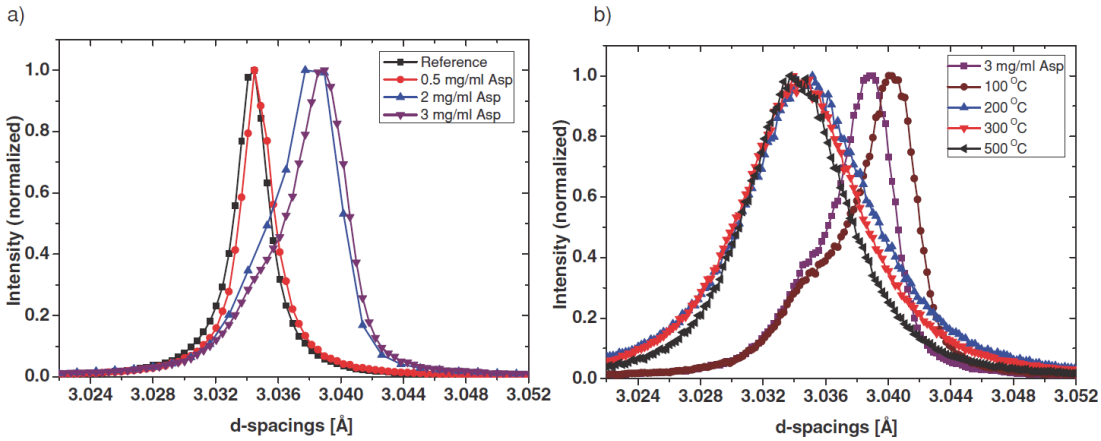

Figure 3–4. The (104) calcite reflections in XRD profiles obtained from the crystals synthesized in the presence of aspartic acid. (a) The concentration of added aspartic acid is 0.5 mg/ml (red), 2 mg/ml (blue) and 3 mg/ml (violet). Black shows a reference calcite powder prepared under the same condition and without the addition of aspartic acid. (b) The concentration of added aspartic acid is 3 mg/ml (violet). Brown, blue, red and black are obtained after the synthesized crystals were annealed at 100°C, 200°C, 300°C and 500°C, respectively. (Borukhin et al., 2012).

aspartic acid. According to Figure 3–4a, higher concentration of aspartic acid in crystal growth solution enlarges the d-spacing of calcite. Figure 3–4b indicates the d-spacing gradually gets back to the value of geological calcite by annealing the synthesized crystals, which means lattice distortion caused by aspartic acid become relaxed. Recently Kim et al. (2011) incorporated anionic diblock copolymer micelles as pseudo-proteins into calcite crystals, which also possessed lattice distortion and furthermore showed the property of inhibiting calcite {104} cleavages. Thus calcite crystals containing insoluble OMs exhibit a monolithic single-crystalline feature, whereas soluble OMs can modify the crystal structure by interacting with calcite lattice.

In this study, I examined the microstructures of synthetic calcium carbonate crystals with intracrystalline soluble OMs extracted from biogenic calcite, in order to clarify the influence of the OMs on crystal structure. As biogenic calcite, I adopted that constituting the prismatic layers of two bivalve shells, *Pinctada fucata* and *Atrina pectinata*, because their crystallographic features are considerably different in spite of their morphological similarity as described in Chapter 2. Each prism of *Pinctada* is composed of several smaller domains of a few micrometers, and shows a polycrystalline feature (Watabe and Wada, 1956; Dauphin, 2003; Okumura et al., 2010), whereas the prisms of *Atrina* have a single-crystalline feature (Dauphin, 2003). At a smaller scale, the prisms of *Pinctada* have sub-grains of several hundred nanometers which are separated by small-angle misorientation caused by intracrystalline OMs, whereas those of *Atrina* are monolithic single crystals without crystal defects and lattice strain. Such structural differences were reproduced to some extent in my synthetic experiments, demonstrating the importance of soluble OMs for building or forming specific crystallographic microstructures in biogenic calcite crystals.

3.2 Materials and methods

Materials

I used the shells of *Pinctada* and *Atrina* for obtaining intracrystalline soluble OMs to add to a crystal growth solution. After their soft inner parts were removed, the shells were dried, then calcite prismatic layers were mechanically separated from nacreous layers.

Preparation of SAMs

To mimic biomineralization processes, template-mediated crystallization is frequently utilized because many biominerals are formed on the templates of insoluble OMs via inhomogeneous nucleation. Among various artificial templates, self-assembled monolayers (SAMs) were often used recently (Aizenberg et al., 1999a, 1999b; Travaille et al., 2002, 2003; Han and Aizenberg, 2003). The templates such as SAMs offer more-regulated crystal growth and serve to understand the influence of soluble OMs on crystal growth. In the present study, the SAMs of a thiol with a carboxyl group (11-mercaptoundecanoic acid, $HS(CH_2)_{10}CO_2H$, Aldrich) were used as template layers. Gold-coated coverslips (Phasis), a {111}-oriented Au thin film of 50 nm thick/a Ti thin film of 5 nm thick for promoting adhesion/borosilicate glass, were used as substrates for the SAMs (Figure 3–5). Just before immersion in a solution of the thiol to form the SAMs, the substrates were cleaned with a strongly oxidizing chemical, a piranha solution (H_2SO_4 : 30% H_2O_2 = 7 : 3), for 15 minutes. The SAMs were formed on the

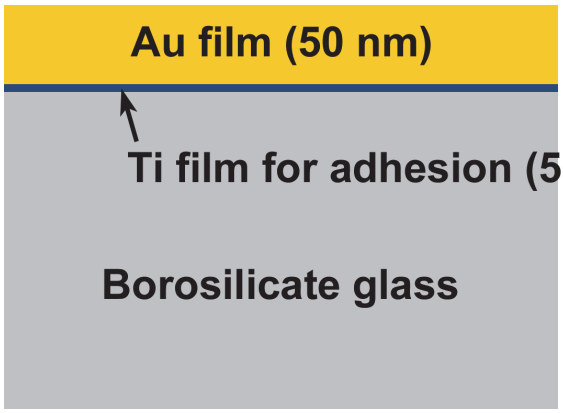

Figure 3–5. Schematic of gold-coated coverslips.

substrates by immersing them in a 5 mM solution of the thiol in ethanol for one week. The atmosphere over the solution was replaced with inert argon gas during the immersion. The resulting surfaces were rinsed with ethanol and dried under an argon gas flow.

Extraction of intracrystalline OMs

The intracrystalline OMs, which were used as organic additives in the synthetic experiments, were extracted by dissolving the calcite prisms of the shells using EDTA. The prismatic layers were preliminarily bleached by an NaClO solution, until their interprismatic organic walls were completely dissolved and individual prisms separated from one another. The separated prisms (0.5 g) were decalcified by a 0.5 M EDTA and a 0.01 wt.% sodium azide (NaN_3) solution (70 mL) at 4°C for one week. According to the gel-filtration column chromatography, the EDTA-soluble fractions of both *Pinctada* and *Atrina* scarcely contain proteins whose molecular weight is less than 30 kDa (Figure 3–6). Then the EDTA-soluble fractions were concentrated by ultrafiltration (Amicon Ultra centrifugal filter unit with a molecular weight cutoff 30 kDa, Millipore), and

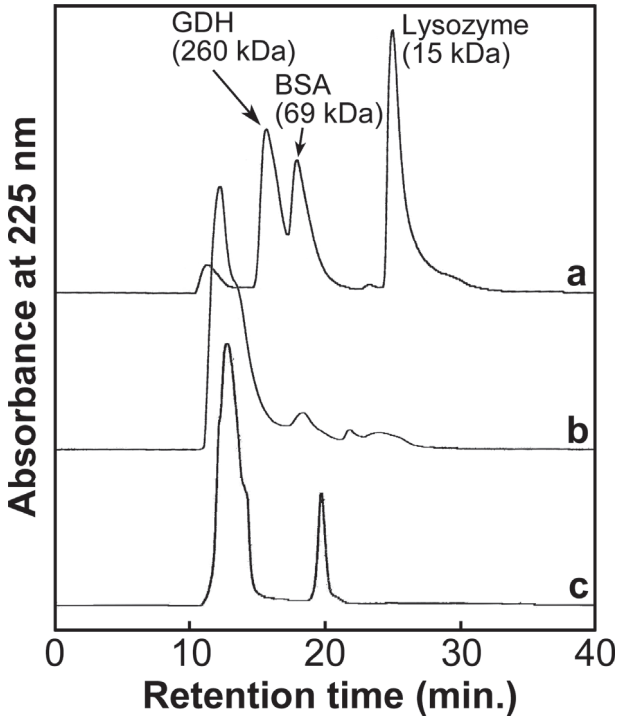

Figure 3–6. Gel-filtration column (KW-803, Shodex) chromatography. Elution was performed with 50 mM phosphate buffer (pH 7.0) at a flow rate of 0.5 ml/min. (a) HPLC elution profile of authentic proteins. Arrows indicate the retention time of each protein. (GDH: glutamate dehydrogenase; BSA: bovine serum albumin). HPLC elution profile of the intracrystalline OMs extracted from *Pinctada* (b) and *Atrina* (c).

desalted by a 10 mM Tris-HCl (pH 8.0) buffer. Finally, remained insoluble materials were filtered out using a 0.45 μm cutoff filter. The concentration of the intracrystalline OMs extracts was measured using a NanoDrop 1000 spectrophotometer (Thermo Fisher Scientific).

Synthetic procedures

The substrates with the SAMs were placed upside-down in 2 mL of a 10 mM calcium chloride ($CaCl_2$) solution with 10 μg/mL OMs extracts. The initial pH of the $CaCl_2$ solution was adjusted to approximately 8.7 with a 10 mM sodium hydroxide (NaOH) before mixing. Instead of the OMs extracts, a 10 μg/mL sodium polyacrylate (PANa, Mw ≈ 2100, Aldrich) solution whose pH was also adjusted to 8.7 with the NaOH was added for control experiments. The vials containing the solutions were placed in a

closed desiccator with another vial containing 1 g of crushed ammonium carbonate [$(NH_4)_2CO_3$]. The precipitation of calcium carbonate crystals was achieved by the diffusion of carbon dioxide (CO_2) vapor into the solution, with the following reactions:

$$(NH_4)_2CO_3(s) \rightarrow 2NH_3(g) + CO_2(g) + H_2O$$

$$CO_2 + Ca^{2+} + H_2O \rightarrow CaCO_3(s) + 2H^+$$

$$2NH_3 + 2H^+ \rightarrow 2NH_4^+$$

Thus $(NH_4)_2CO_3$ not only provides CO_2 to the solution, but also prevents pH change of the solution by the formation of ammonium ions. The crystal growth was carried out at room temperature for one day. After the reaction, the substrates were recovered from the solution and gently rinsed with ultrapure water, and dried under an argon gas flow. Additionally, the calcium carbonate crystals precipitated in the solution were also collected, washed three times with ultrapure water and twice with ethanol, air-dried, and analyzed using XRD.

SEM observation

SEM observation was carried out using an S-4500 SEM (Hitachi) with a cold field-emission gun at an acceleration voltage of 5 kV. SEM specimens were coated with Pt–Pd before observation.

TEM observation

The specimens for TEM examination were prepared using an FB-2100 FIB system with a micro-sampling system (Hitachi High-Technologies). The specimens were locally

coated with tungsten for preventing beam damage during fabrication, and trimmed using a gallium ion beam of 30 kV, and then thinned down to be electron-transparent with a low energy beam of 10 kV as a final process. TEM was conducted using a JEM-2010UHR TEM (JEOL) operated at 200 kV, in order to observe the crystallographic features of calcite and the distribution of the OMs inside the crystals, which were imaged by the Fresnel contrasts.

STEM–EELS analysis

EELS analysis was conducted using an Enfina spectrometer (Gatan) equipped to a JEOL JEM-2010F TEM (JEOL) with a field-emission gun operated at 200 kV, in order to verify that Fresnel contrasts in the crystals correspond to organic matter. Specimens were prepared using FIB in the same manner as those for TEM observation, and cleaned using a JIC-410 ion cleaner (JEOL) just before the analyses to avoid contaminations. Since each Fresnel contrast was very small, EELS spectra were obtained from nanoscopic areas (< 10 nm) by converging an electron beam in a STEM mode. Each spectrum was collected within 5 seconds to avoid radiation damage, and approximately 30 spectra were collected and integrated with attention to an energy shift.

XRD analysis

As complementary and macroscopic characterization of the crystallographic aspect, XRD analysis was also conducted. Powder XRD patterns were obtained using a RINT-Ultima^{+} diffractometer (Rigaku) with Cu Kα radiation emitted at 40 kV and 30

mA. A D/teX Ultra module with a silicon strip detector (Rigaku) was equipped to the instrument. Cu Kβ was eliminated by Ni foil. To improve the signal-to-noise ratio, a nonreflecting silicon sample holder was used. A 0.25° divergence slit, a 5 mm mask for confining the beam width, and an 8 mm anti-scatter slit were adopted. A scan rate was 0.1° (2θ)/min and data was collected at every 0.01° (2θ). Local lattice strain ($\Delta d/d$) and coherence length (L) was estimated using Williamson–Hall plots. Detailed analytical procedures are described in Chapter 2A. The synthesized calcite crystals were examined three times to estimate the error of measurements.

Amino acid composition analysis

Aliquots of the OMs extracts were lyophilized and hydrolyzed under vacuum in 2 mL of a 6 N hydrochloric acid (HCl) at 110°C for one day after flushing twice with nitrogen. Following evaporation of the HCl, the hydrolysates were analyzed on an L-8900 amino acid analyzer (Hitachi) with ninhydrin detection.

3.3 Results

3.3.1 SEM observation

As mentioned above, I adopted SAMs as the substrates for crystallization and prepared SAMs of $HS(CH_2)_{10}CO_2H$ on Au {111}, on which calcite crystals are expected to nucleate with {11l} planes as an interface (Han and Aizenberg, 2003). In my

experiments, however, the interface plane was obviously not {11*l*} but {012} (Figure 3–7a and 7e). Although the origin of this difference is not clear, the nucleation was regulated by the substrates because the interface plane is uniform. When the OMs extracts from the shells were added to the system, regardless of those from *Pinctada* or *Atrina*, the interface planes of almost all precipitated crystals changed to {104} (Figure 3–7b, 7c and 7f). When the organic additive was PANa, the calcite crystals with the interface planes of both {012} and {104} were precipitated on the SAMs, indicating that PANa is less influential in crystal nucleation than the extracted OMs (Figure 3–7d–f). With regard to the size, the crystals synthesized with the OMs from *Atrina* and with PANa are smaller than those with the OMs from *Pinctada* and without any additives. As for the shapes, all crystals with organic additives are rounded off, but do not have clear differences depending on the additives.

3.3.2 TEM observation

TEM specimens were prepared from the synthesized crystals on the SAMs using FIB and observed along a_i-axes of calcite. In the BF image captured under a strong diffraction condition, the crystals without any organic additives exhibited a monolithic single-crystalline feature because bend contours are smooth and continuous (Figure 3–8a). The crystals synthesized with the soluble OMs from *Atrina* and with PANa are also perfect single crystals (Figure 3–8e and 8g). By contrast, defect-induced contrast was observed in the crystals synthesized with those from *Pinctada* (Figure 3–8c), implying that the OMs extracted from *Pinctada* interact more strongly with the calcite crystals to induce crystal defects. In the under-focused images, Fresnel contrasts were

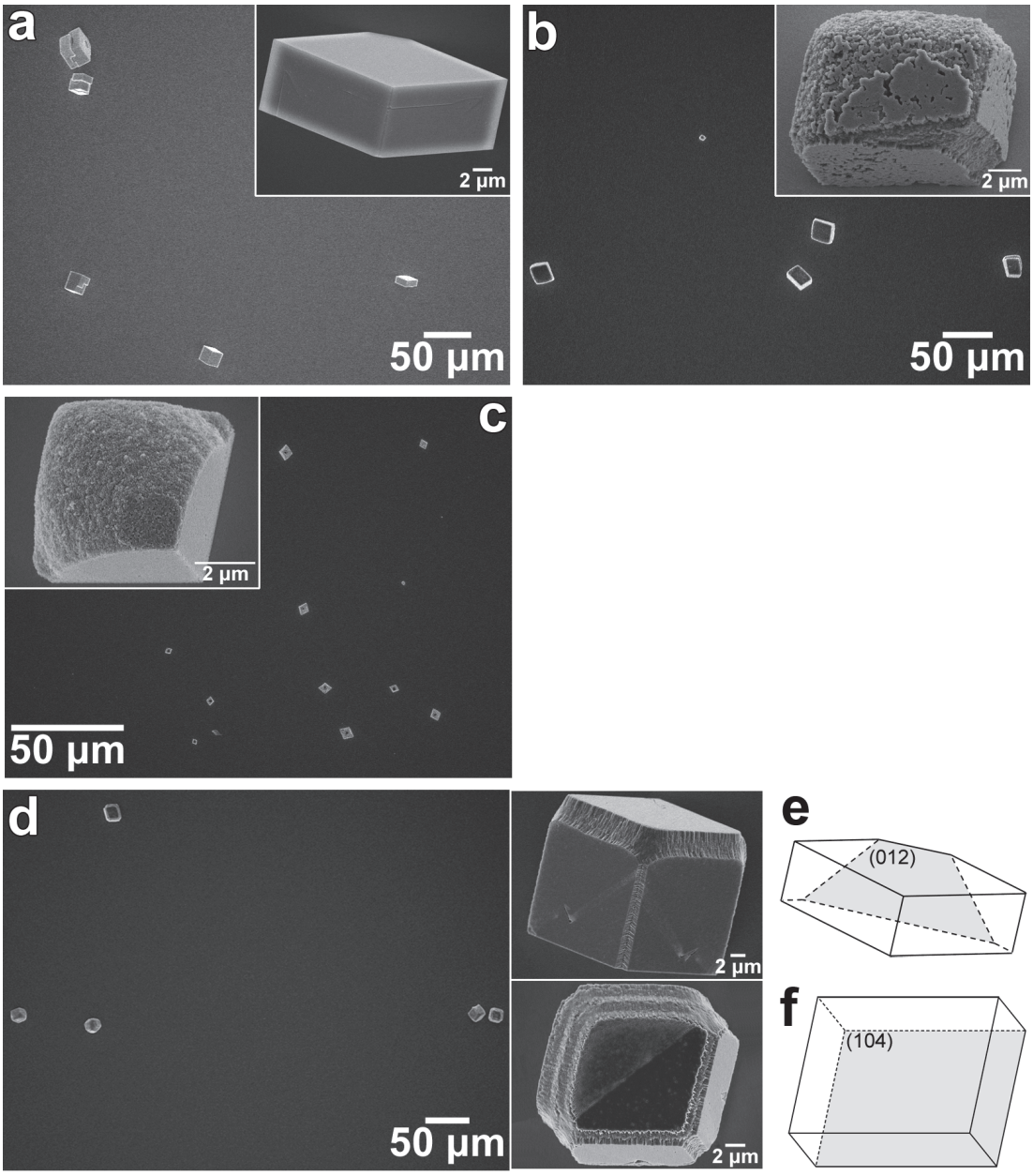

Figure 3–7. SEM images of calcite crystals and enlarged views of one of the crystals, which were synthesized without additives (a), and in the presence of the intracrystalline soluble OMs extracted from *Pinctada* (b), from *Atrina* (c), and PANa (d). Schematic illustrations of calcite on SAMs with interface planes as {012} (e) and {104} (f).